



Microstructure, Mechanical Properties, and Corrosion Behavior of Mg–Al–Ca Alloy Prepared by Friction Stir Processing

Wen Wang¹ · Shan-Yong Chen¹ · Ke Qiao¹ · Pai Peng¹ · Peng Han¹ · Bing Wu¹ · Chen-Xi Wang¹ · Jia Wang¹ · Yu-Hao Wang¹ · Kuai-She Wang¹

Received: 28 May 2021 / Revised: 13 June 2021 / Accepted: 15 June 2021 / Published online: 14 September 2021
© The Chinese Society for Metals (CSM) and Springer-Verlag GmbH Germany, part of Springer Nature 2021

Abstract

Friction stir processing (FSP) was used to modify the microstructure and improve the mechanical properties and corrosion resistance of an Mg–Al–Ca alloy. The results demonstrated that, after FSP, the grain size of the Mg–Al–Ca alloy was decreased from 13.3 to 6.7 μm . Meanwhile, the Al_8Mn_5 phase was broken and dispersed, and its amount was increased. The yield strength and ultimate tensile strength of the Mg–Al–Ca alloy were increased by 17.0% and 10.1%, respectively, due to the combination of fine grain, second phase, and orientation strengthening, while the elongation was slightly decreased. The immersion and electrochemical corrosion rates in 3.5 wt% NaCl solution decreased by 18.4% and 37.5%, respectively, which contributed to grain refinement. However, the stress corrosion cracking (SCC) resistance of the modified Mg–Al–Ca alloy decreased significantly, which was mainly due to the filiform corrosion induced by the Al_8Mn_5 phase. SCC was mainly controlled by anodic dissolution, while the cathodic hydrogen evolution accelerated the SCC process.

Keywords Friction stir processing · Mg–Al–Ca alloy · Second phase · Mechanical properties · Stress corrosion cracking

1 Introduction

Mg–Al–Ca alloys are widely used in the automotive, electronics, and aerospace fields, to manufacture parts, such as automobile drivelines, engine blocks, and automatic transmission cases, due to their low cost, high specific strength, and excellent casting properties [1–5]. However, the strength and plasticity of Mg–Al–Ca alloys are low due to their hexagonal close-packed (HCP) lattice structure. Furthermore, the negative electrode potential of magnesium (Mg) is low (-2.37 V), which limits the further application of Mg–Al–Ca alloys. Recent works have shown that grain refinement is an effective method for improving

the mechanical properties and corrosion resistance of Mg–Al–Ca alloys [1, 6, 7].

Currently, many severe plastic deformation (SPD) technologies, such as extrusion, rolling, and multi-directional forging [2, 6–10], are used to prepare fine-grained Mg–Al–Ca alloys. However, these fine-grained Mg alloys prepared through the above SPD technologies have many limitations, such as poor microstructural uniformity, high dislocation density, and low plasticity and corrosion resistance [11, 12]. Therefore, for purpose of improve the mechanical properties and corrosion resistance of fine-grained Mg alloys, it is necessary to search for a more suitable method.

Recently, friction stir processing (FSP) has been introduced, which is a new SPD technique developed based on friction stir welding [13]. The principle of FSP is simple. First, a tool with a shoulder and a pin rotates into the workpiece. After the pin has been completely inserted into the workpiece, and the shoulder is in touch with the workpiece surface, the rotating tool moves along the predetermined direction. Under the synergetic effect of the pin and the shoulder, thermoplastic materials undergo severe plastic deformation, which results in dynamic recrystallization and significant grain refinement. FSP can break up, refine, and homogenize the grains and the second phase

Available online at <http://link.springer.com/journal/40195>.

✉ Ke Qiao
qiaoke_2020@126.com

✉ Kuai-She Wang
wangkuaishe888@126.com

¹ School of Metallurgical Engineering, National and Local Joint Engineering Research Center for Functional Materials Processing, Xi'an University of Architecture and Technology, Xi'an 710055, China

of Mg alloys simultaneously, leading to fine-grained materials with high strength and good plasticity [14–16]. At present, several researchers have prepared fine-grained AZ31, AZ80, and WE43 Mg alloys by FSP [17–20]. Wang et al. [18] used FSP to refine the grains of an as-cast AZ31 Mg alloy, and the results revealed that the network-like β -Mg₁₇Al₁₂ was broken up and dissolved rapidly, which improved the ultimate tensile strength (UTS) and elongation (El). Liu et al. [21, 22] found that after FSP of as-cast AZ91 and Mg-9Al-xRE alloys, the second phases were broken and dispersed under the effect of severe friction, which enhanced the passivation effect of corrosion product film and improved corrosion resistance. In addition, Huang et al. [19, 23] reported that the grain refinement and dissolution of the second phases could improve the stress corrosion cracking (SCC) resistance of FSP AZ80 Mg alloys. The above results demonstrated that FSP can improve the mechanical properties and corrosion resistance of Mg alloys.

The mechanical properties of Mg–Al–Ca alloys modified by FSP have been evaluated by several researchers [24]. For example, Nene et al. [25] performed FSP on as-cast AXM541 Mg alloys and found that both the grain and second phase refinement promoted the UTS of the Mg alloy. However, the effect of microstructure evolution on the corrosion resistance of Mg–Al–Ca alloys modified by FSP is not clear yet. Furthermore, in practical applications, materials are often subjected to stress in corrosive environments. The SCC resistance of Mg–Al–Ca alloys under the effect of stress and corrosive environment has not been investigated so far. Consequently, the effect of microstructural evolution on the mechanical properties and SCC of Mg–Al–Ca alloys after FSP was assessed in this work.

2 Experimental

2.1 Material and Processing

In this study, as-extruded Mg–Al–Ca alloy plates (chemical composition, Mg-2.4Al-0.8Ca-0.4Mn-0.7Zn by wt%) with dimensions of 200 mm × 80 mm × 6 mm (length × width × thickness) were selected as the base material (BM). Figure 1 illustrates a schematic diagram of FSP. The processing direction is parallel to the extrusion direction. The FSP process was conducted at a rotation speed of 1000 rpm and processing speed of 300 mm·min⁻¹. A H13 stir tool with a double circular shoulder of 15 mm in diameter combined a concave pin of 5.5 mm in length, with a diameter of 3 mm and 7.5 mm at the top and root, respectively, was used.

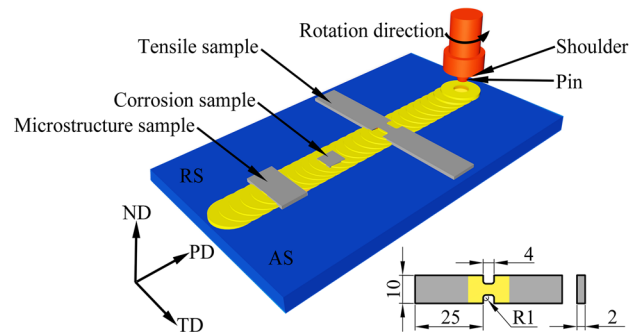


Fig. 1 Sampling position and dimensions of the samples used for the microstructure observations, tensile tests, and corrosion experiments (units: mm). AS represents the advancing side, and RS represents the retreating side. PD, TD, and ND represent the processing, transversal, and normal directions, respectively

2.2 Microstructure Characterization

Samples for microstructure characterization with dimensions of 20 mm × 6 mm × 5 mm (length × width × thickness) were cut along the transverse direction (Fig. 1). The microstructure was observed through scanning electron microscopy (SEM, Gemini SEM 300) after the samples were polished and etched in a solution (5 g of picric acid, 5 mL of acetic acid, 90 mL of ethanol, and 10 mL of distilled water) for 10 s. The grain size, high- and low-angle grain boundaries (HAGBs/LAGBs), and textures were characterized by electron back-scattering diffraction (EBSD, Gemini SEM 300). The EBSD samples were mechanically polished and electrolytically etched with a corrosion solution (15 mL perchloric acid and 85 mL ethanol) at a voltage of 8 V, current density of 5×10^{-3} A·mm⁻², and temperature of -30 °C for 200 s. The second phase was analyzed by X-ray diffraction (XRD, Bruker D8 Advance) with Cu K α radiation ($\lambda = 0.15406$ nm) at 40 kV and transmission electron microscopy (TEM, TALOS F200X) equipped with energy-dispersive spectroscopy (EDS). The TEM samples were cut from the stirring zone (SZ) and BM, ground to a thickness of 35–50 μ m, and were twin-jet polished in a solution with 3 vol.% perchloric acid and 97 vol.% alcohol at -25 °C before observation.

2.3 Tensile Test

The sampling position and sample size are presented in Fig. 1, and the parallel section of tensile samples is located in the SZ. Tensile testing was conducted using an Instron 8801 tensile testing machine at an initial strain rate of 1×10^{-3} s⁻¹. Each test was repeated at least three times to guarantee data accuracy. After the tensile tests, the fracture surface of the samples was observed by SEM.

2.4 Weight Loss Test

Weight loss test samples with dimensions of 6 mm × 6 mm × 3 mm (length × width × thickness) were taken from the BM and SZ (Fig. 1). The test surface was ground, polished, and dried, while the non-test surface was encapsulated with silica gel and soaked in 3.5 wt% NaCl solution for 3 h, 6 h, 12 h, 24 h, and 48 h. The corrosion products were cleaned by an acidic solution (CrO₃(200 g/L) + AgNO₃ (10 g/L) + H₂O (1 L)), and the silastic was removed after the weight loss test. The corrosion rate, P_w (mm/y), was calculated according to Eq. (1).

$$P_w = 2.10 \frac{|W_0 - W_t|}{St}, \quad (1)$$

where W_0 (g) and W_t (g) are the weight of the samples before and after soaking, respectively, and S (cm²) and t (d) are the corrosion area and immersion time, respectively.

2.5 Electrochemical Corrosion Test

The electrochemical corrosion test was performed on Gamry Reference 600 + electrochemical workstation in 3.5 wt% NaCl solution and used a typical three-electrode system. The sampling position and dimensions were same as those of the weight loss test. The FSP samples were served as the working electrode, while a platinum sheet and saturated calomel electrode were served as the counter electrode and the reference electrode. The potentiodynamic polarization curves were obtained under a scanning rate of 1.0 mV/s over a potential range from −2 to −1 V. The corrosion rate P_i (mm/y) was calculated according to Eq. (2) [26].

$$P_i = 22.85 i_{\text{corr}}, \quad (2)$$

where i_{corr} (mA/cm²) represents the corrosion current density.

2.6 Stress Corrosion Test

The SCC sensitivity was evaluated by slow strain rate tensile (SSRT) tests with an initial strain rate of $1 \times 10^{-6} \text{ s}^{-1}$. The corrosion medium were air and 3.5 wt% NaCl solution. The sample dimensions were the same as those of the tensile tests. Each test was repeated at least three times to guarantee data accuracy. The SCC sensitivity indices were calculated according to the followings:

$$I_{\text{SCC}}(\text{UTS}) = \left[1 - \frac{\delta_{\text{sol}}}{\delta_{\text{air}}} \right], \quad (3)$$

$$I_{\text{SCC}}(\epsilon) = \left[1 - \frac{\epsilon_{\text{sol}}}{\epsilon_{\text{air}}} \right], \quad (4)$$

where $I_{\text{SCC}}(\text{UTS})$ and $I_{\text{SCC}}(\epsilon)$ are the SCC sensitivity indices of UTS and EI, respectively, δ_{sol} and δ_{air} (MPa) are the UTS in NaCl solution and air, respectively, and ϵ_{sol} and ϵ_{air} are the EI in NaCl solution and air, respectively. The closer the stress corrosion sensitivity index to 1, the higher the stress corrosion sensitivity of the sample. After the SSRT tests, the fracture surface of the samples was observed by SEM.

3 Results

3.1 Macrostructure

Figure 2 depicts the cross-sectional macrostructures of the FSP samples. A basin-shaped, dense, and compact SZ can be observed evidently. The profile on both sides of the SZ appears asymmetric, which is attributed to the different flow direction of the material on the AS and RS.

3.2 Microstructure

Figure 3 presents the EBSD images of the BM and FSP samples. The grain size distribution of the BM and FSP samples ranged between 1–38 μm and 1–20 μm, respectively, while their average grain size was 13.3 μm and 6.7 μm, respectively (Fig. 3a, b). The percentages of the HAGBs and LAGBs for the BM samples were 81.0% and 19.0%, respectively, while those for the FSP samples were 43.6% and 56.4%, respectively (Fig. 3c, d). Clearly, the LAGB percentages of the FSP samples were higher than those of the BM due to the formation of dislocation substructures during FSP [11].

Figure 4 presents the SEM images of the BM and FSP samples. The second phase of the BM sample was mainly distributed along the grain boundary with an average size of 3.0 μm (Fig. 4a), while that of the FSP sample was dispersed over the grain boundary and the intragranular

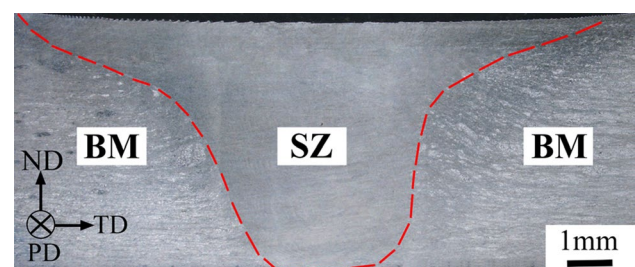


Fig. 2 Cross-sectional macrostructure of the FSP sample

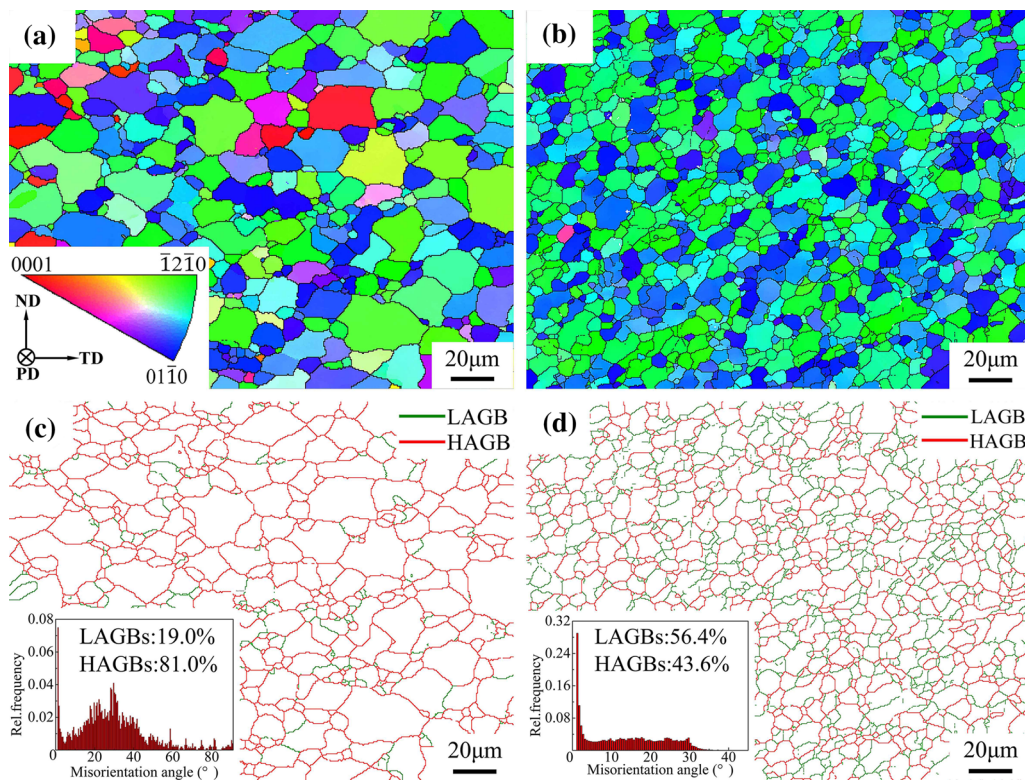


Fig. 3 Grain morphologies **a, b**, grain boundaries distributions **c, d** of BM and FSP samples

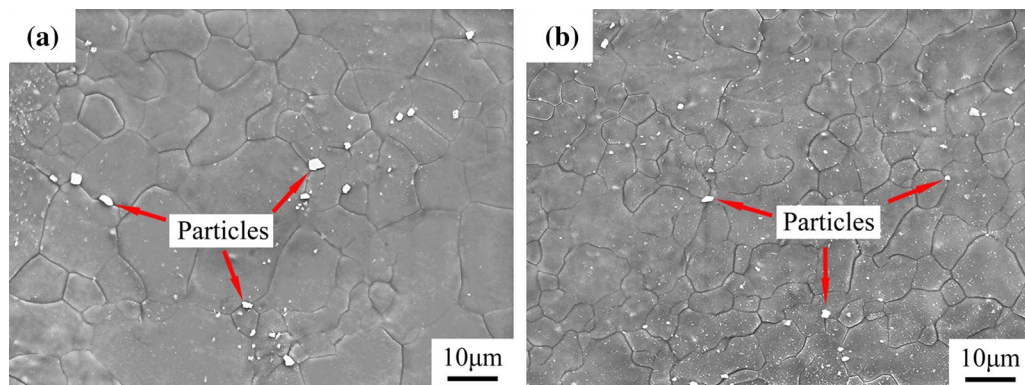


Fig. 4 SEM images showing the second phase particles of the **a** BM, **b** FSP samples

region, and the average size was decreased to 1.1 μm (Fig. 4b). Apparently, the number of second phase particles in the FSP sample was much higher than that of the BM sample.

In Fig. 5, the bright-field TEM images and EDS maps reveal the element distribution of the BM and FSP samples. The size of the dispersed second phase in the matrix of the FSP sample was smaller than that of the BM sample (Fig. 5a, b). The EDS results demonstrated that the ratio of Al to Mn elements was close to 8:5 for P1 and P2 in Fig. 5a, b, respectively (Table 1).

The XRD patterns of the BM and FSP samples are shown in Fig. 6. It can be observed that both the BM and FSP samples were composed of $\alpha\text{-Mg}$ and Al_8Mn_5 phase. Nevertheless, the peak of the Al_8Mn_5 phase for the FSP sample was more apparent, and its half-peak breadth was larger than that of the BM. This indicated that, in the FSP sample, the amount of the Al_8Mn_5 phase was much higher and its size was smaller than those in the BM sample. The results were consistent with Fig. 5.

Figure 7 demonstrates the pole figures and Schmid factor (SF) distribution of the basal slips in the TD direction of the

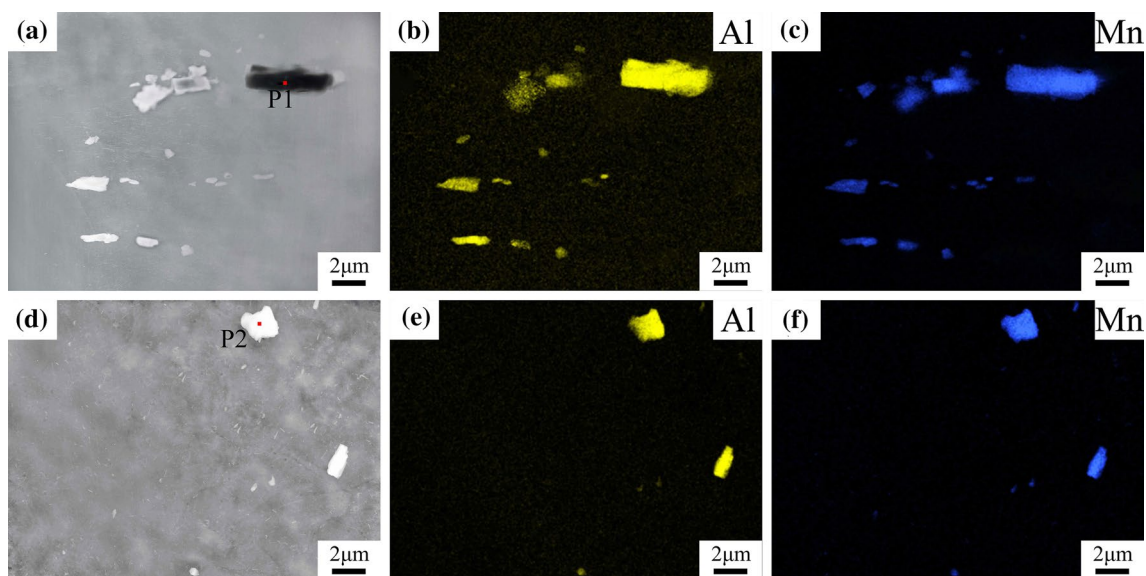


Fig. 5 Bright field TEM images and EDS maps of the a–c BM, d–f FSP samples

Table 1 Atomic percent of P1 and P2 in Fig. 5a and b, respectively (at.%)

Points	Mg	Al	Mn	Ca	Zn
P1	5.36	54.45	40.00	0.01	0.17
P2	6.51	59.68	33.58	0.06	0.16

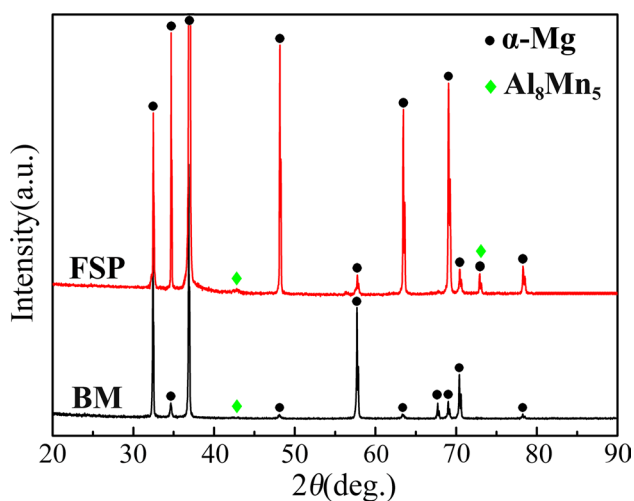


Fig. 6 XRD patterns of the BM and FSP samples

BM and FSP samples. BM sample exhibited an obvious texture with its *c*-axis being approximately parallel to the ND, and the maximum polar density was 12.9 (Fig. 7a). During FSP, most grains deflected under the strong rotating extrusion effect of the pin, with the *c*-axis deviating 15°–30° away

from the ND to the PD, and the maximum polar density increased to 75.5 (Fig. 7b). Furthermore, the average SF of the BM and FSP samples along the TD was 0.20 and 0.07, respectively (Fig. 7c, d). Consequently, the grain orientations of the FSP sample can hinder the base slip, which is defined as a “hard orientation.”

Figure 8 demonstrates the engineering stress–strain curves of the BM and FSP samples. It can be observed that the yield strength (YS), UTS, and El of the BM sample were 106 MPa, 276 MPa, and 41.1%, respectively, while those of the FSP sample were 124 MPa, 304 MPa, and 39.0%, respectively (Fig. 8a). Compared to the BM samples, the YS and UTS of the FSP samples were higher by 17.0% and 10.1%, respectively, while the El was slightly lower.

3.3 Weight Loss Test

Figure 9 presents the P_w values (calculated according to Eq. (1)) of the BM and FSP samples after immersion. Two main results can be obtained. First, the P_w values of both the BM and FSP samples decreased with increasing corrosion time. In addition, the P_w values of both the BM and FSP samples were high in the first 12 h, and as the corrosion time increased, corrosion products were accumulated on the surface, hindering the contact between solution and matrix alloy, and inhibiting the corrosion process. Therefore, the curves tended gradually to become flat after 12 h [19]. Second, the lower P_w of the FSP sample indicated the better corrosion resistance compared to the BM sample.

Figure 10 presents the SEM morphologies of the weight loss test samples after being immersed in NaCl solution for 3, 24, and 48 h. After 3 h, a large number of pits were

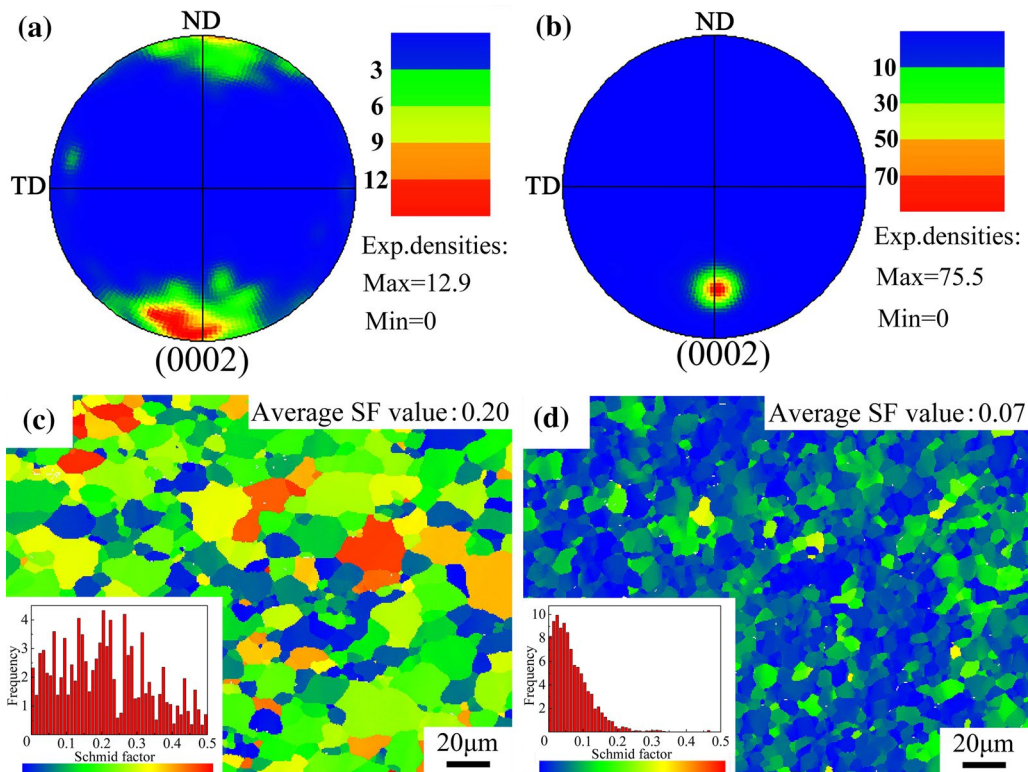


Fig. 7 a, b Pole figures, c, d SF distributions of basal slips along the TD for the BM (left) and FSP (right) samples

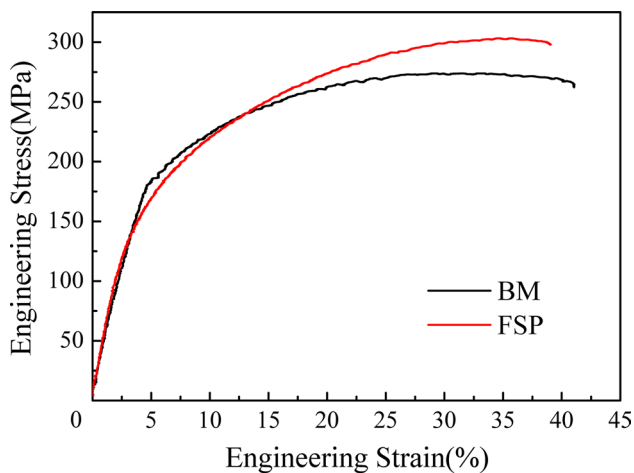


Fig. 8 Engineering stress–strain curves of the BM and FSP samples

generated on the surface of the BM sample (Fig. 10a). After 24 h, the corrosion pits area expanded and the pit depth increased rapidly (Fig. 10b). In addition, the corrosion pits expanded with increasing immersion time and, after 48 h, samples were corroded severely (Fig. 10c). However, a significant difference between the FSP and BM samples occurred. It was found that FSP sample surface generated a few scattered pits after being immersed for

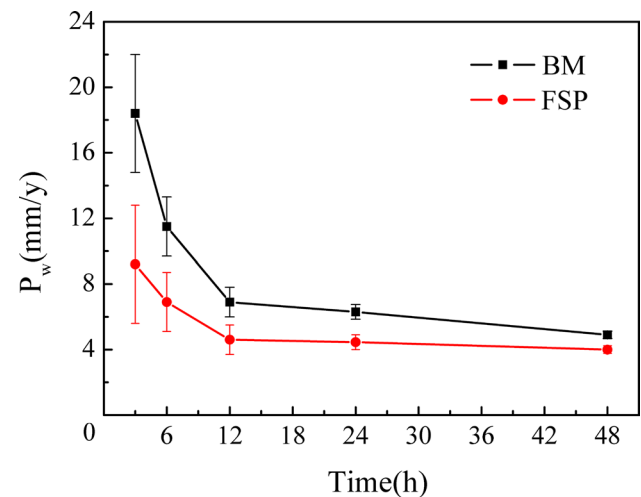


Fig. 9 Corrosion rates of the BM and FSP samples convert from the weight loss

3 h (Fig. 10d). Furthermore, the corrosion pits expanded into fluvial pattern, and the corrosion depth was large. It was observed that the corrosion area of the FSP sample was smaller than that of the BM sample (Fig. 10e). While the edge of the FSP sample expanded and collapsed as the immersion time increased to 48 h, the corrosion area was still flat (Fig. 10f).

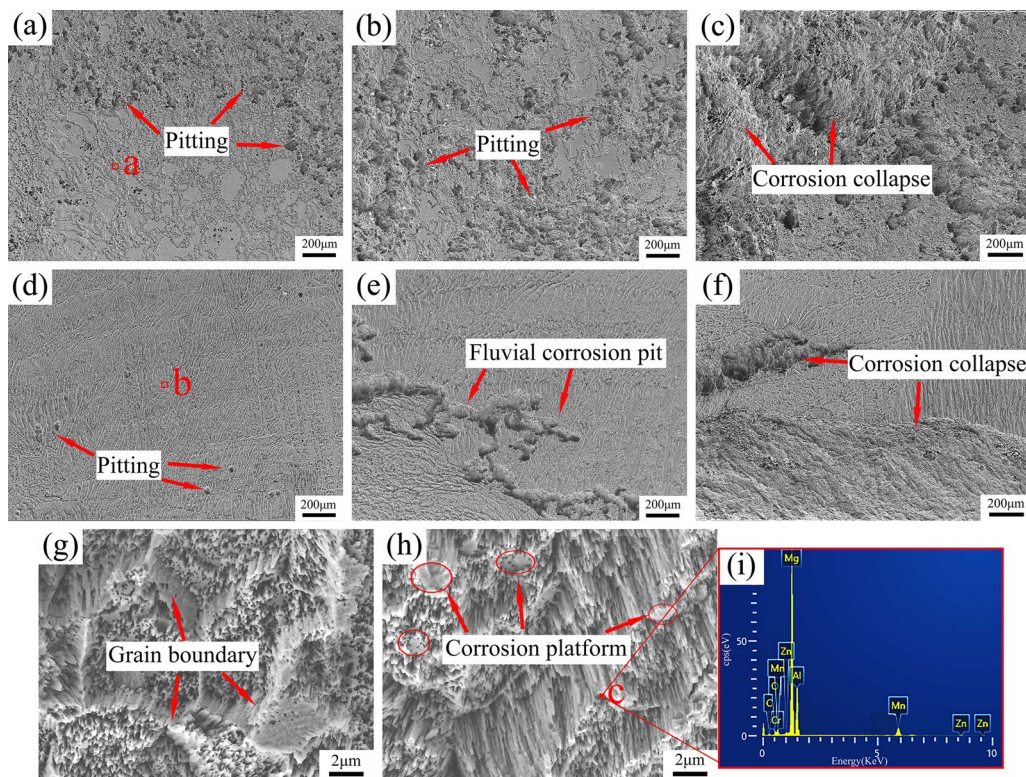


Fig. 10 SEM morphologies after different immersion time: **a, d** 3 h, **b, e** 24 h, and **c, f** 48 h for the BM (first row) and FSP (second row) samples; **g, h** enlarged diagrams of points **a** and **b** in **a, d**, respectively. **i** EDS spectra of point **c** in **h**

Figure 10g, h shows enlarged diagrams of the **a** and **b** region in Fig. 10a, d, respectively. For BM sample, it can be observed that the corrosion within the grains was more severe than that at the grain boundaries, which indicated that a typical intergranular corrosion occurred in the BM sample. Normally, the grain boundaries act as a barrier, which can inhibit corrosion. Thus, a lot of parallel corrosion grooves, round corrosion pits, and platforms were generated on the corrosion surface of the FSP sample. The EDS analysis of point **c** in Fig. 10h revealed that the mass fraction of Al and Mn in the corrosion pits was 25.2 wt% and 11.1 wt%, respectively, indicating that the main components of the corrosion pits were Al_3Mn_5 phase.

3.4 Electrochemical Corrosion Behavior

Figure 11 shows the potentiodynamic polarization curves of the BM and FSP samples in 3.5 wt% NaCl solution. It can be observed that the cathodic curves of the BM and FSP samples almost coincided, indicating that their cathodic corrosion reactions were basically the same. In addition, obvious passivation zones occurred in the anode curves of both samples. The breakdown potential (E_b) of the passive films of the BM and FSP samples was -1.24 V and -1.16 V, respectively, which indicated that the corrosion resistance

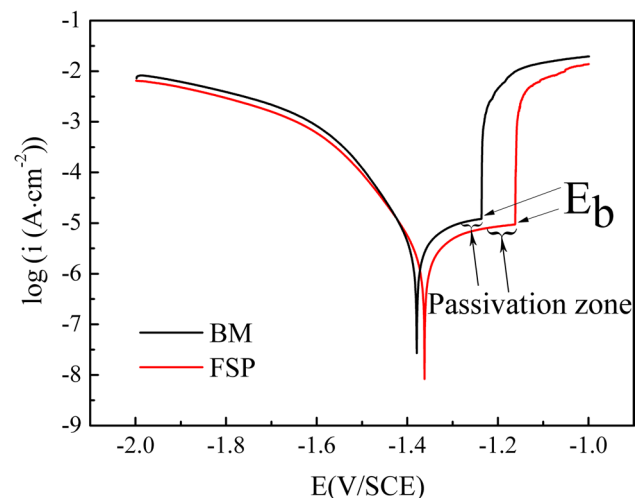


Fig. 11 Potentiodynamic polarization curves of the BM and FSP samples in 3.5 wt% NaCl solution

of the FSP sample was better than that of the BM sample. Table 2 presents the electrochemical data of the corrosion potentials (E_{corr}) and i_{corr} obtained from the polarization curves through Tafel extrapolation. It can be observed that the E_{corr} of the FSP sample was larger than that of the BM sample, while the i_{corr} and P_w were lower than those of the

Table 2 E_b , E_{corr} , i_{corr} and P_i of the BM and FSP samples in 3.5 wt% NaCl solution

Samples	E_b (V)	E_{corr} (V)	i_{corr} (mA cm ⁻²)	P_i (mm y ⁻¹)
BM	-1.24	-1.38	3.4×10^{-3}	0.08
FSP	-1.16	-1.36	2.2×10^{-3}	0.05

BM sample, demonstrating that the electrochemical corrosion resistance of the FSP sample was better than that of the BM sample.

3.5 Stress Corrosion Behavior

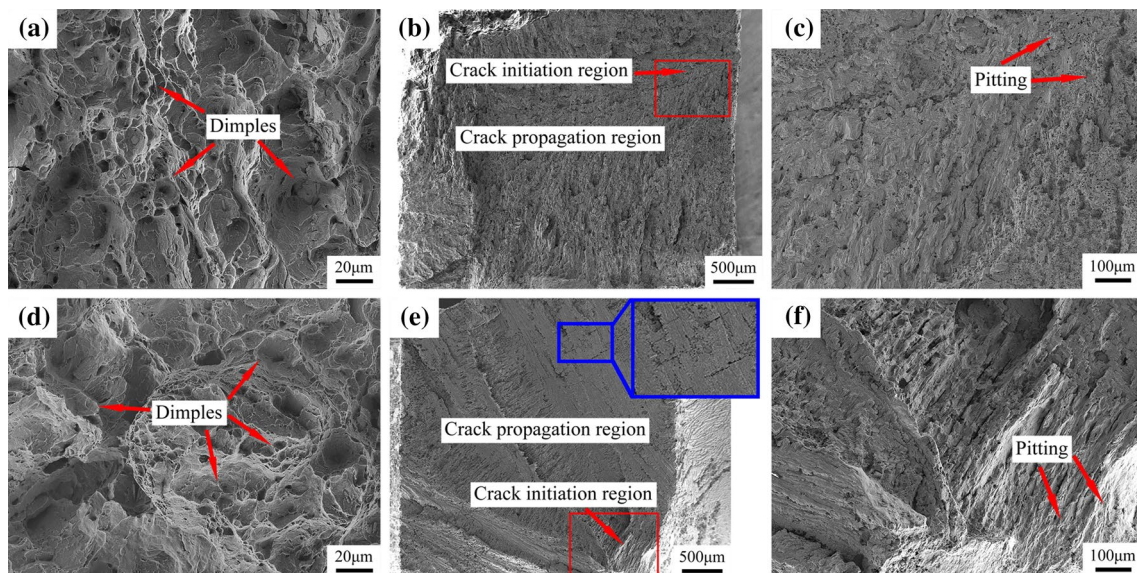
Table 3 presents the SSRT test results and stress corrosion sensitivity indices of the BM and FSP samples. It can be found that the UTS of the BM and FSP samples was 274 MPa and 277 MPa in air, and the EI was 47.6% and 46.5%, respectively. In 3.5 wt% NaCl solution, the UTS of the BM and FSP samples decreased significantly to 220 MPa and 197 MPa, respectively, and the EI decreased to 7.0% and 6.0%, respectively. The I_{SCC} (UTS) of the FSP sample was higher than that of the BM sample, while the

$I_{\text{SCC}}(\epsilon)$ of both samples was similar. The above results indicated that the strength loss of the FSP sample in 3.5 wt% NaCl solution was severe. Furthermore, both the I_{SCC} (UTS) and $I_{\text{SCC}}(\epsilon)$ results revealed that the FSP sample had higher SCC sensitivity than the BM sample.

In Fig. 12, the SSRT fracture morphology of the BM and FSP samples in air and 3.5 wt% NaCl solution is presented. Numerous dimples were observed on the tensile fracture surface of both samples in air, indicating ductile fracture (Fig. 12a). Figure 12b, e presents, respectively, the SCC fracture morphology of the BM and FSP samples in solution. The fracture morphologies of both the BM and FSP samples were exhibited transgranular brittle fracture (Fig. 12b, e), and pitting pits with different size were distributed at the pattern polymerization, indicating that the fracture originated from pitting (Fig. 12c, f). It is worth to mention that the corrosion area at the edge of the FSP sample was smaller than that of the BM sample, while the fracture surface of the FSP sample was smoother than that of the BM sample. In addition, secondary cracks, perpendicular to the crack propagation direction, were observed on the fracture surface of the FSP sample (Fig. 12e). Similar results were reported by Argade et al. [17].

Table 3 SSRT test results and SCC sensitivity indices of BM and FSP samples

Samples	UTS _{air} (MPa)	ϵ_{air} (%)	UTS _{sol} (MPa)	ϵ_{sol} (%)	I_{SCC} (UTS)	$I_{\text{SCC}}(\epsilon)$
BM	274	47.6	220	7.0	0.20	0.85
FSP	277	46.5	197	6.0	0.29	0.87

**Fig. 12** Fracture surfaces of the SSRT test samples: **a, d** in air; **b, e** in solution for the BM (first row) and FSP (second row) samples; **c, f** enlarged diagrams of the selected areas in **b, e**

4 Discussion

4.1 Effect of Microstructure Evolution on Tensile Behavior

Compared to the BM sample, the YS and UTS of the FSP sample were slightly improved. This is mainly attributed to the following aspects: On the one hand, the grain size of the Mg–Al–Ca alloy was refined after FSP (Fig. 3b). According to the Hall–Petch relationship, the finer the grain size, the stronger the grain boundary strengthening effect [15]. On the other hand, according to Jia et al. [27], the Al_8Mn_5 phase does not precipitate or dissolve during the FSP process, but, under the action of severe friction and stirring, it can be broken up and dispersed, thus increasing the number of Al_8Mn_5 particles (Fig. 4). Therefore, the strengthening effect of the second phase can be critically improved [16]. In addition, basal slip is the main deformation mechanism of Mg alloys at room temperature, and the orientation also plays an important role in their plastic deformation [11]. The basal slip SF of the FSP sample along the TD was 0.07, which was significantly lower than that of the BM (0.20), resulting in orientation strengthening. Luo et al. [28] performed FSP on AZ61 Mg alloys and their results revealed that the UTS and EI were significantly improved due to grain and second phase refinement, as well as the high proportion of HAGBs. In summary, the combination of fine grain, second phase, and orientation strengthening can improve the YS and UTS of FSP samples.

Figure 13 compares the UTS and EI of FSP and Mg–Al–Ca alloys prepared by rolling, extrusion, and forging [2, 6–10]. It can be observed that the UTS of the Mg–Al–Ca alloy prepared by FSP was higher than that obtained after

extrusion and rolling; however, it was lower than that obtained after multi-directional forging. Nene et al. and Chai et al. [16, 23] investigated the strengthening mechanism of FSP Mg–Al–Ca alloys and demonstrated that the contribution of grain refinement strengthening was higher than that of second phase strengthening. Compared to that of the FSP sample (6.7 μm), the grain sizes of the rolling samples (11 μm [6], 19 μm [7], 8 μm [9]) and extrusion samples (9.7 μm [2] and 13 μm [10]) were coarsened, while those prepared by multi-directional forging (1.14 μm and 2.39 μm [8]) were refined, which was the main reason for the different mechanical properties between FSP and other technologies. Moreover, the EI of the Mg–Al–Ca alloy prepared by FSP was better than that of alloys prepared by other technologies. Wang et al. [14] found a similar phenomenon in FSP Mg alloys, because FSP Mg alloys have higher proportion of HAGBs that induces high plasticity. Similarly, Chai et al. [16, 29] reported that grain boundary sliding is the main mechanism of plastic deformation, and HAGBs and uniform fine grains can coordinate plastic deformation and improve the EI.

4.2 Effect of FSP on Static Corrosion Behavior

The results in the present study demonstrated that the static corrosion resistance of the FSP samples was significantly improved compared to that of the BM due to the fined Al_8Mn_5 particles. First, compared to the BM sample, the grain size of the FSP sample was clearly fined (from 13.3 to 6.7 μm), which improved the density and adhesion of the passive film on the substrate, thus hindering the corrosion damage. Wang et al. [30] reported that grain refinement is beneficial to the formation of a uniform and dense passive film, which enhances the corrosion resistance. Furthermore, Wu et al. [31] suggested that the grain boundary not only acts as a corrosion barrier, but also provides sites for the nucleation of the passive films, while the higher grain boundary density is conducive to passive film formation, thus improving the corrosion resistance. Second phases also have a great effect on the corrosion rate of Mg alloys. For the second phases, they act as cathode to α -Mg, will form a microcouple with α -Mg, and induce the formation of local corrosion. However, for the second phases that can enhance the passivability of corrosion products of magnesium alloys, such as Al–Re and Mg–Al, the dispersion of them will promote uniform corrosion. Liu et al. [21, 22] investigated that after FSP, second phases were broken and distributed in the alloy, which increases the passivation of corrosion products. Therefore, the corrosion resistance of the AZ91 and Mg-9Al-xRE alloys was improved. In this study, the potential of Al_8Mn_5 was 600 mV, which is lower than that of the α -Mg matrix. Therefore, the Al_8Mn_5 phase particles act as cathodes during the corrosion process, forming galvanic

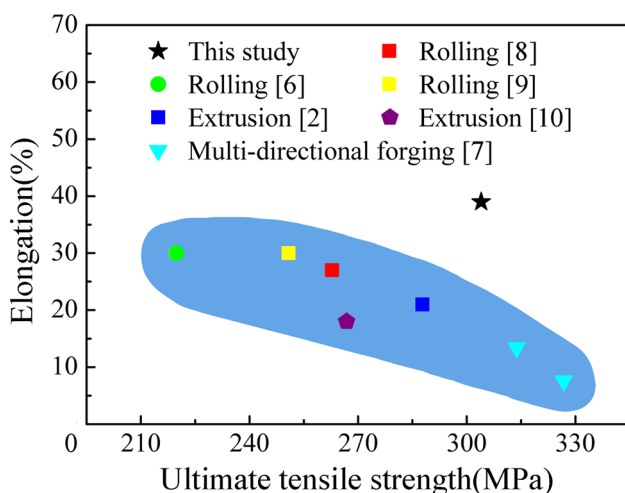
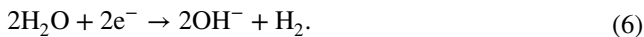


Fig. 13 UTS and EI comparison of Mg–Al–Ca alloys prepared through different SPD technologies

cells with the α -Mg matrix phase and resulting in pitting formation and expansion [32]. Compared to the BM sample, the Al_8Mn_5 particles of the FSP sample were finer and exhibited a higher distribution density, which induced filiform corrosion during the corrosion process (Fig. 10e). Similarly, Bahmani et al. [8] also reported that the second phase, which acts as cathode with the α -Mg matrix, reacts with the adjacent matrix to accelerate the corrosion of the matrix and induce pitting expansion into the filiform corrosion.

4.3 Effect of FSP on SCC Behavior

Figure 14 exhibits the SCC mechanism of the BM and FSP samples in NaCl solution. It can be observed that a film of corrosion product covered on the surface of the samples and then dissolved into the NaCl solution. The base alloy was exposed to the solution under the synergistic effect of applied load and Cl^- . Under these conditions, the Mg matrix formed galvanic cells with the passive film, leading to anodic dissolution. Moreover, the Al_8Mn_5 particles also formed galvanic cells with α -Mg, accelerating the anodic dissolution. During the dissolution process, Mg^{2+} and H_2 are generated according to the following reactions [30, 33–35]:



As shown in Fig. 14, SCC occurred when the stress concentration at the bottom of the corrosion pits. Huang et al. [23] reported that in the initial stage of SCC, the corrosion products cover the surface of the corrosion pits, playing a passivation role. As the corrosion process progressed, the Cl^- and external load broke the passive film, which led to

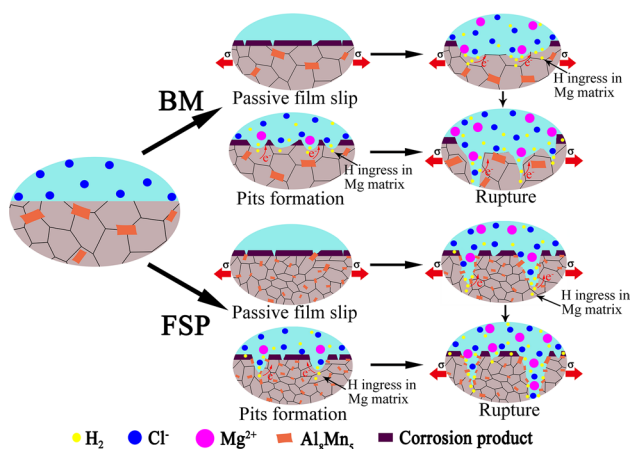


Fig. 14 Schematic illustration of the proposed SCC mechanism of the BM and FSP samples

aggravation of Mg matrix corrosion and SCC. Moreover, the hydrogen released from the cathode diffused into the Mg alloy matrix and accelerated SCC. Atrens et al. [36] demonstrated that the diffusivity of hydrogen in Mg alloys can reach $10^{-9} \text{ m}^2 \text{ s}^{-1}$ – $10^{-5} \text{ cm}^2 \text{ s}^{-1}$, which can release a large number of hydrogen atoms to the crack tip that will diffuse to the lattice of the Mg alloy. In addition, Huang et al. [23] and Kannan et al. [37] investigated the SCC behavior of AZ80 and AZ31 Mg alloys and their results revealed that the diffusion of hydrogen atoms induced a large number of secondary cracks on the fracture surface, which aggravated the SCC. In the present study, secondary cracks perpendicular to the crack propagation direction were observed on the fracture surface of the FSP sample (Fig. 12e). The results revealed that the SCC of the BM and FSP samples were mainly induced by anodic dissolution and cathodic hydrogen evolution.

According to the results in this study, the UTS and El sensitivity indices of the FSP sample were higher than those of the BM sample, which indicated the FSP samples have poor SCC resistance. Previous studies have shown that grain refinement is conducive to improving SCC resistance. For instance, Huang et al. [19] demonstrated that grain refinement can increase the grain boundary area and hinder SCC propagation, thus improving the SCC resistance. Additionally, Ge et al. [38] proved that the positions where dislocation slip occurred facilitate SCC initiation, and the ability of fine grains to hinder dislocation slip is stronger, which improve SCC resistance. Nevertheless, this explanation cannot justify why, in this study, the SCC of the FSP samples deteriorated. In this work, high-density Al_8Mn_5 particles were observed in the FSP samples, which caused the pitting corrosion to expand and form filiform corrosion. Under the action of tensile stress, the local stress concentration around the filamentous corrosion pits was more likely to generate a large number of microcracks, which would propagate until fracture. Similarly, Argade et al. [39] presented that the second phase of the cathode formed a microcell with the Mg alloy matrix, which promoted the intergranular cracking of stress corrosion.

5 Conclusions

1. After FSP, the average grain size of the Mg–Al–Ca alloy was refined from 13.3 to 6.7 μm , and the grain refinement mechanism was dynamic recrystallization. In addition, after FSP, the HAGBs decreased from 81.0 to 43.6% and the Al_8Mn_5 phase was broken up and dispersed.
2. FSP increased the YS and UTS by 17.0% and 10.1% to 124 MPa and 304 MPa, respectively. The main strength-

ening mechanisms were fine grain, second phase, and orientation strengthening.

3. After FSP, the immersion and electrochemical corrosion properties of the Mg–Al–Ca alloy were improved, mainly due to grain refinement. The decreased SCC resistance was mainly attributed to the filamentous corrosion of FSP sample. The SCC of the Mg–Al–Ca alloy was mainly controlled by anodic dissolution induced by the Al_8Mn_5 phase, and the released hydrogen accelerated the SCC.

Acknowledgements This work was financially supported by the National Natural Science Foundation of China (Nos. 52034005, U1760201, 51974220), the National Key Research and Development Program of China (No. 2017YFB0306202), the Key Research and Development Program of Shaanxi Province (No. 2017ZDXM-GY-037), the Youth Innovation Team of Shaanxi Universities (2019–2022), and the China Baowu Iron and Steel Group Co. Ltd with Mg–Al–Ca alloy materials.

References

- [1] G. Han, D. Chen, G. Chen, J. Huang, *J. Mater. Sci. Technol.* **34**, 2063 (2018)
- [2] X. Liu, X. Qiao, Z. Li, M. Zheng, *Mater. Charact.* **162**, 110197 (2020)
- [3] S.W. Xu, K. Oh-ishi, S. Kamado, H. Takahashi, T. Homma, *Mater. Sci. Eng. A* **542**, 71 (2012)
- [4] A.V. Koltygin, V.E. Bazhenov, E.A. Belova, A.A. Nikitina, J. Magnes, *Alloys* **1**, 224 (2013)
- [5] S.W. Xu, N. Matsumoto, K. Yamamoto, S. Kamado, T. Honma, Y. Kojima, *Mater. Sci. Eng. A* **509**, 105 (2009)
- [6] M.Z. Bian, T.T. Sasaki, B.C. Suh, T. Nakata, S. Kamado, K. Hono, *Scr. Mater.* **138**, 151 (2017)
- [7] M.Z. Bian, T.T. Sasaki, T. Nakata, S. Kamado, K. Hono, *Mater. Sci. Eng. A* **730**, 147 (2018)
- [8] A. Bahmani, S. Arthanari, K.S. Shin, *Int. J. Adv. Manuf. Technol.* **105**, 785 (2019)
- [9] U. Masood Chaudry, T. Hoo Kim, S. Duck Park, Y. Sik Kim, K. Hamad, J.G. Kim, *Materials* **11**, 2201 (2018)
- [10] T. Nakata, C. Xu, R. Ajima, K. Shimizu, S. Hanaki, T.T. Sasaki, L. Ma, K. Hono, S. Kamado, *Acta Mater.* **130**, 261 (2017)
- [11] Y.Y. Jin, S.K. Wang, W. Wang, P. Peng, S. Zhou, L. Huang, T. Yang, K. Qiao, B. Zhang, J. Cai, H.L. Yu, *Mater. Charact.* **150**, 52 (2019)
- [12] G. Liu, Z. Ma, G. Wei, T. Xu, X. Zhang, Y. Yang, W. Xie, X. Peng, *J. Mater. Process. Technol.* **267**, 393 (2019)
- [13] R.S. Mishra, Z.Y. Ma, *Mater. Sci. Eng. R* **50**, 1 (2005)
- [14] W. Wang, P. Han, P. Peng, T. Zhang, L.Q. Wang, S.N. Yuan, L.Y. Huang, H.L.Yu.K. Qiao, K.S. Wang, *Acta Metall. Sin. -Engl. Lett.* **33**, 43 (2019)
- [15] B. Mansoor, A.K. Ghosh, *Acta Mater.* **60**, 5079 (2012)
- [16] F. Chai, D. Zhang, Y. Li, J. Magnes, *Alloys* **3**, 203 (2015)
- [17] G.R. Argade, W. Yuan, K. Kandasamy, R.S. Mishra, *J. Mater. Sci.* **47**, 6812 (2012)
- [18] W. Wang, K.S. Wang, Q. Guo, N. Wu, *Rare Met. Mater. Eng.* **41**, 1522 (2012)
- [19] L.Y. Huang, K.S. Wang, W. Wang, Y.Y. Jin, K. Qiao, T. Yang, P. Peng, T.Q. Li, *Eng. Fail. Anal.* **92**, 392 (2018)
- [20] J. Li, D.T. Zhang, F. Chai, W. Zhang, *Rare Met.* **39**, 1267 (2014)
- [21] Q. Liu, Q.X. Ma, G.Q. Chen, X. Cao, S. Zhang, J.L. Pan, G. Zhang, Q.Y. Shi, *Corros. Sci.* **138**, 284 (2018)
- [22] Q. Liu, G.Q. Chen, S.B. Zeng, S. Zhang, F. Long, Q.Y. Shi, *J. Alloys Compd.* **851**, 156835 (2020)
- [23] L.Y. Huang, K.S. Wang, W. Wang, P. Peng, K. Qiao, Q. Liu, *Mater. Corros.* **71**, 93 (2019)
- [24] N. Xu, R. Feng, Q. Song, Y. Bao, *J. Mater. Res. Technol.* **8**, 4448 (2019)
- [25] S.S. Nene, S. Zellner, B. Mondal, M. Komarasamy, R.S. Mishra, R.E. Brennan, K.C. Cho, *Mater. Sci. Eng. A* **729**, 294 (2018)
- [26] C. Zhang, L. Wu, G. Huang, Y. Huang, B. Jiang, A. Atrens, F. Pan, *J. Alloys Compd.* **823**, 153884 (2020)
- [27] Y. Jia, J. Hou, H. Wang, Q. Le, Q. Lan, X. Chen, L. Bao, *J. Mater. Process. Technol.* **278**, 116542 (2020)
- [28] X.C. Luo, L.M. Kang, H.L. Liu, Z.J. Li, Y.F. Liu, D.T. Zhang, D.L. Chen, *Mater. Sci. Eng. A* **797**, 139945 (2020)
- [29] F. Chai, D. Zhang, Y. Li, W. Zhang, *Mater. Sci. Eng. A* **568**, 40 (2013)
- [30] B.J. Wang, D.K. Xu, J. Sun, E.H. Han, *Corros. Sci.* **157**, 347 (2019)
- [31] P. Wu, F. Xu, K. Deng, F. Han, Z. Zhang, R. Gao, *Corros. Sci.* **127**, 280 (2017)
- [32] S.M. Baek, H.J. Kim, H.Y. Jeong, S.D. Sohn, H.J. Shin, K.J. Choi, K.S. Lee, J.G. Lee, C.D. Yim, B.S. You, H.Y. Ha, S.S. Park, *Corros. Sci.* **112**, 44 (2016)
- [33] R. Zeng, W. Dietzel, R. Zettler, W. Gan, X. Sun, T. Nonferr, *Metal. Soc.* **24**, 3060 (2014)
- [34] R. Xin, B. Li, L. Li, Q. Liu, *Mater. Des.* **32**, 4548 (2011)
- [35] P. Metalnikov, G. Ben-Hamu, K.S. Shin, *Met. Mater. Int.* **27**, 1493 (2019)
- [36] A. Atrens, N. Winzer, G. Song, W. Dietzel, C. Blawert, *Adv. Eng. Mater.* **8**, 749 (2006)
- [37] M. Bobby Kannan, W. Dietzel, R. Zeng, R. Zettler, J.F. dos Santos, *Mater. Sci. Eng. A* **460–461**, 243 (2007)
- [38] M.Z. Ge, J.Y. Xiang, L. Yang, J.T. Wang, *Surf. Coat. Technol.* **310**, 157 (2017)
- [39] G.R. Argade, S.K. Panigrahi, R.S. Mishra, *J. Mater. Sci.* **55**, 1216 (2019)